United States Geological Survey

National Earthquake Hazard Reduction Plan

External Grants Program Announcement G14AP00068

Award Number: G14AP00068

Final Technical Report

The Role of Fault Bends and Complexities in Earthquake Ruptures: Empirical Relations for Use in Seismic Hazard Analysis

Glenn P. Biasi[1] and Steven G. Wesnousky[2]

University of Nevada Reno

Seismological Laboratory MS 0174

Reno, NV 89557

[1]Tel.: (775) 784-4576, Fax: 775-784-4165,

Email: glenn@unr.edu

[2]Tel.: (775) 784-6067, Fax: 775-784-4165,

Email: wesnousky@ unr.edu

Award Period: June 1, 2014 - May 31, 2016

Abstract

We examine 67 surface rupture maps for map-scale complexities including fault bends, discontinuous rupture, overlaps, and fault-to-fault rupture. We find that these structural properties of faults influence the likelihood of rupture propagation and estimates of magnitude of future ruptures. Angles of bends at ends of surface ruptures on strike slip faults are systematically larger than interior bends, while corresponding populations are similar for dip-slip events. The probability of passing a bend in a strike slip rupture increases systematically with the bend angle in a relationship roughly summarized by the passing ratio $PR = 3.0 – 0.077*A$, where A is the bend angle. Bends of 26° are passed or stop rupture with about equal probability. Maximum interior bend angles and net orientation change of rupture ends are reasonably explained by frictional resistance and an approximately constant orientation of regional stress. The average curvature of a fault rupture is defined by dividing the sum of absolute values of bends in rupture by rupture length. Curvatures of strike-slip ruptures concentrate below 1°/km, with a maximum of 1.7°/km; dip slip curvatures are 3 times larger. Overlaps in dip slip ruptures are commonly expressed as secondary offsets of the hanging wall, and on average cover a larger fraction of rupture length than strike slip ruptures. We find that most fault-to-fault rupture connections jump to a fault of like mechanism. Only two strike-slip ruptures out of a total of 42 jump to reverse structures and continue for a significant length. Results here could improve rupture length estimates in fault seismic hazard assessment and provide data for validation of dynamic models of rupture.

Introduction

The state of practice for estimating seismic hazard from active faults has advanced to the point that non-characteristic behavior and fault-to-fault connectivity in earthquakes commonly form part of the analysis. The Uniform California Earthquake Rupture Forecast 3 recognized these issues in developing earthquake probabilities for California (UCERF3; Field et al., 2014). In UCERF3, ruptures on faults are allowed to assume almost any length, and fault-to-fault connectivity in ruptures are allowed if the connection satisfies criteria concerning geometric compatibility and maximum separation distance (Milner et al., 2013). Fewer possible ruptures are considered in a typical site-specific fault source characterization, but problems remain in assessing how faults connect, how far long ruptures may reach and thus how large earthquakes can get, and how to estimate the relative probabilities among possible earthquakes on an individual fault or network of faults.

Fault geometry can be used to constrain hazard estimates. A “characteristic” magnitude can be estimated from the fault length, down-dip width. Empirical observation (Lettis et al., 2002; Wesnousky, 2006; Biasi and Wesnousky, 2016) and dynamic modeling (Harris and Day, 1993; Duan and Oglesby, 2006; Scholz et al., 2010; Lozos et al., 2011; Lozos et al., 2014) find that steps in faults often arrest rupture, and thus their presence can be used to adjust probabilities among lengths of expected earthquakes. Other research on non-planar faults has been conducted by Harris et al. (1991), Aochi et al. (2000), Anderson et

al. (2003), Kame et al. (2003), Oglesby et al. (2003), Kase and Day (2006), Oglesby (2008), Ando et al. (2009), Bhat et al. (2007) and Fliss et al. (2005). Fault bends may influence or arrest rupture because they are associated with changes in fault friction, elastic and gravitational energy, and inelastic rock deformation (Scholz, 2002). Saucier et al. (1992) relate the sinuosity of the fault trace to degrees of concentration of fault-perpendicular stresses, which on scales of a few km relate to relative readiness of rupture to propagate. Duan and Oglesby (2007) find that rupture propagation through a geometric offset also depends on the fault rupture history. Ruptures may be arrested for some number of cycles, but cause progressive damage that leads ultimately to successful through rupture. The state of the fault relative to failure is typically unknown, so for a given step, currently they must be approached as a statistical probability. A step "passing ratio" relationship was developed for this purpose from empirical data (Biasi and Wesnousky, 2016). It suggests that the success ratio depends on step size. Step size is thus a fault geometry measurement that can be used to improve seismic hazard estimates.

Lozos et al. (2011) use fault rupture dynamic models to conduct a comprehensive parametric study of steps and, indirectly, bends in fault rupture. In their model two main fault sections of vertical strike-slip fault are set parallel to one another, but offset by varying distances. Connecting the two, they add a relay fault at an angle that is systematically varied. For small separation distances the angle of the relay had little effect – rupture dynamics of the system essentially overwhelm the resistance. As the separation between main sections increases, the relay fault becomes longer, and like a fault bend that the rupture must overcome to continue on the other side of the step. For relays of 7 km the bend angle systematically influences rupture propagation. They also find that the alignment of the model driving stress relative to the bend section affects the possibility of rupture propagating through the bend. For stresses aligned to drive the main fault, compressional bends up to about 18° and extensional bends up to 34° are consistently passed. With a 10° rotation of the stress field in a direction favorable to the compressional step, threshold angles switch, and compressional bends up to 31° are passed by all ruptures, while extensional bends pass only up to 18°. Overall, their study predicts that strike-slip ruptures should rarely pass through bends larger than ~34° for bends characterized by lengths ≥7 km.

Data and Methodology

Biasi and Wesnousky (2016) and Wesnousky (2008) developed synthesis maps of 75 surface ruptures. These maps present ruptures in a common format at a scale adequate for interpretation of fault bends with branches of 5 km or greater. Associated metadata including rupture length, earthquake magnitude, and rupture mechanism were also compiled. The present study applies these maps and assembled data to study the effect of bends on surface ruptures. In this study we:

(1) Analyze and tabulate angles of bends inside and at the ends of ruptures;
(2) Measure of the total and net angular deviations of ruptures for comparison to similar bounds implemented in UCERF3;
(3) Compile instances of "Y" and disjoint rupture, and fault-to-fault rupture types; and

(4) Tabulate and analyze rupture overlap lengths.

Of the total map set, 67 ruptures are long enough and their maps detailed enough to provide data on rupture behavior at fault bends. The data are comprised of 42 strike-slip, 11 reverse, and 14 normal mechanism ruptures. Slip mechanism type was assigned on the basis of dominant slip at the surface. Oblique slip in some events may account for response at fault bends transitional between norms for pure strike-slip and dip-slip ruptures.

Rupture Bend Complexities

In this section we describe measurements and empirical relationships among rupture features that affect propagation. **Figure 1** illustrates measurements made on surface ruptures. These include interior angles overcome in rupture, angles associated with rupture termination, net orientation change comparing rupture ends, total absolute angular deflection, and lengths of rupture overlap. The angle measurements themselves are described more completely below. In making these measurements, a suitable scale length must be considered. Features smaller than a km or so are inconsistently recorded in the original surface rupture maps, especially for the larger and older ruptures. We instead summarize rupture orientation and bends in terms of linear portions at least 5-7 km in length. This is approximately the scale used in the UCERF3 model. By adapting this scale length, results from this study may thus be useful in future versions of UCERF. The scale length also affects how we interpret bends at rupture ends. In many cases especially for strike-slip faults, ruptures end with some displacement on an oblique dip-slip structure. For accounting of fault-to-fault propagation, we attempted to capture the main sense of the rupture. For example, a strike-slip surface rupture that dies after a few km continuance on a high-angle structure was generally not considered a fault-to-fault rupture.

Maximum Angles Passed Inside Ruptures

Interior bends (IBs) are angles through which a rupture succeeds in propagating (e.g., θ_1 and θ_2 in Figure 1h). The largest absolute angle deflections (Max IB) through which rupture is observed to propagate for each respective earthquake in Table 1 are plotted in **Figure 2**. **Figure 2a** shows interior bends for strike-slip and dip-slip ruptures as a function of surface rupture length. Longest strike slip ruptures may show a weak trend toward smaller Max IB, but overall, Max IB does not obviously depend on rupture length. **Figure 2b** plots the same Max IB data in the form of a cumulative distribution. Dip-slip and strike-slip populations are seen to differ as measured by Max IB, with median values of 17° and 38°, respectively. Over 95% of largest bends in strike-slip ruptures strongly concentrate below 28°, with only two exceptions above this: the Denali, 2002 rupture at the Denali-Susitna Glacier strike-slip-reverse junction and the 1957 Gobi-Altai rupture, where a 15 km salient projects out of strike with the main rupture. Maximum IB measures in dip-slip ruptures concentrate below 50°, but at all percentiles include larger interior bends than do strike-slip ruptures.

Angular Deflections Stopping Rupture

Surface ruptures have been observed with field mapping to sometimes end at high-angle oblique structures or at significant bends in fault strike. To quantify the frequency of this phenomenon, angle deflections associated with rupture termination are plotted in **Figure 3**. Ruptures from **Tables 1** and **2** may contribute 2, 1, or 0 data points to the plot, depending on how the rupture ends and whether map relations are clear. Largest fault deflections are concentrated among ruptures less than ~105 km, but if we qualitatively adjust for data density, there is no obvious trend of the size of bends at rupture terminations with rupture length among either dip-slip or strike-slip mechanisms. Such a pattern might be expected if longer ruptures require larger angular deflections to stop them. To quantify the relative incidence of ending deflections of various sizes, **Figure 3b** presents ending angles as cumulative fractions. For strike-slip ruptures, a smooth distribution of ending deflection angles is observed, with 90% being less than 60°. Fewer data are available for dip-slip ruptures, but the measurements indicate that ending at a deflection are rarely less than 20°. It is not clear why dip slip ruptures would generally have a minimum deflection angle.

Net Angular Deflection (NAD).

The NAD is defined here as the absolute difference in map orientation between the two ending sections of a surface rupture (Figure 1h). Ruptures for input to the UCERF3 Grand Inversion were limited to NAD<60° (Milner et al., 2013) as a way to limit pathological fault-to-fault cases. Historical ruptures provide an empirical measure of how variable the NAD may be in nature.

Figure 4 shows the net angular deflection for the combined surface rupture set. The measurement of NAD attempts to capture the main sense of the rupture, so minor normal or reverse terminal structures on primary strike-slip ruptures were not included in the NAD (**Figure 1**). The four NAD measurements greater than 50° (**Figure 4a**) are all associated with dip slip ruptures. The largest of these occurred in the 2011/04/11 Fukushima-ken Hamadori earthquake, where rupture proceeded north on the Itozawa fault, then continued southeast through a net angle of 147° on the Yunodake fault. Only three of 42 strike-slip ruptures have an NAD greater than 31°. Of these, only one, the 1943 Tosya, Turkey, event is associated with bending on a relatively simple fault trace. The others (1992 Landers, and 2002 Denali) involve significant fault-to-fault complexities. By comparison, 30% of dip-slip ruptures have ends 30° or more from each other.

Total Deflections

The total absolute angular deflection (TAAD) is a measure of rupture complexity. TAAD is measured as the sum of the absolute value of angular deflections in a rupture trace (TAAD = $|\theta_1|+|\theta_2|$ in Figure 1h). We measure it using the 5-7 km length scale adopted for this project. UCERF3 familiarly referred to the TAAD as "squirreliness" since it arose as a measure of frequency of orientation change. UCERF3 limited ruptures considered credible to a maximum of 560° (Milner et al., 2013). Since bends in ruptures

are associated with changes in friction, momentum, and rupture energetics, empirical measurement of TAAD provides one measure of how much change actual ruptures overcome.

We summarize observations of total absolute angular deflection in **Figure 5**. The TAAD increases with rupture length at first because some length is needed for each section to reach minimum length to count in a bend (**Figure 5a**). Continued growth of TAAD with rupture length might be expected if ruptures gain length by breaking past more bends, but this pattern is not observed. The one exceptional event among strike-slip ruptures, with a TAAD of 257°, is the 1957 Gobi-Altai earthquake (Choi et al., 2012). In this case the TAAD seems to be due to the strong oblique component of rupture. Systematic differences between the dip-slip and strike-slip populations are clear when plotted as complimentary cumulative distributions (**Figure 5b**), with TAADs for dip-slip ruptures being roughly twice the corresponding values for strike slip. TAAD can be recast into a measure of average curvature by dividing TAAD by the rupture length (**Figures 5c, 5d**). Measured in this way, the dip-slip rupture population strongly separates from the strike-slip set, with median curvatures of 1.6°/km versus 0.5°/km, respectively. We note that because the TAAD sums the absolute values of orientation changes, the average curvature in ruptures will not, in general, apply to the full rupture length.

Ending vs. Passed Angle Deflections

For estimating fault hazards it would be useful to know the relative effectiveness of fault bends to stop ruptures. This can be developed by comparing the relative incidence of a bend angle in the sample from the ends of ruptures to its frequency among interior bends passed during rupture. For example, if bends of 15° form a large fraction of interior bends, but a small fraction of those stopping rupture, then we would conclude that a 15° bend is not a strong barrier to rupture. Data for this comparison are shown on **Figure 6** and repeated from **Figures 2** and **3**. In **Figure 6a** the basic properties of the comparisons can be seen. The median rupture ending bend is 26°, compared to a median interior bend of ~13°. Maximum interior bends are also shown in **Figure 6.** Since by definition they have been overcome in rupture, they provide a limiting sample for comparison to rupture ending bends. The corresponding data for dip slip ruptures in **Figure 6b** does not suggest the same degree of predictability as strike slip. For example, the maximum interior bends are systematically larger than the bends ending rupture. At face value this means that, when examining a fault for candidate ruptures, that a steep bend is more often passed than stops a rupture.

To actually compare effectiveness of bends to stop ruptures, we compare the relative fractions formed by bends of a given size among interior bends and bends ending ruptures. Since the sample sizes are relatively small, we count bends in non-overlapping 5° bins, with centers at 7.5°, 12.5°, etc. The fractions of data in each bin are shown in **Figures 7a and 7b** for the strike slip and dip slip subsets. Bin fractions for rupture ending do not quite add to 1.0 because some data are in bins outside the range shown. The ratio of bin weights of interior to ending bends contains the desired information of how frequently a given bend stops rupture (**Figure 7c**). With a ratio of over 2:1, bends

less than 13 degrees are passed inside rupture, compared to stopping rupture. For a bend of 32 degrees the ratio is reversed, and rupture stops more often than it continues. The small sample sizes lead to scatter, but the trend to declining passing ratio with increasing bend angle is clear. Using data from 5 to 40°, a linear trend $PR=3.0 – 0.077A$ is found, where PR is the passing ratio, and A is the bend angle. This trend cannot be to be linear for all angles, since it predicts meaningless negative passing ratios for bends greater than about 40°. We note that the relationship for PR should not be interpreted over-precisely. A steeper line would result using only data from 5-35°; modestly adjusted values would result if different bin widths or bin centers were used. All original measurements are provided in **Table 1**.

Dip slip data do not yield as simple a trend for passing ratio. For example, bends greater than 40° are passed at higher ratios than they stop rupture. However, if we use the data in **Figure 7b** to summarize more coarsely, bends in the three bins less than 20° are passed as a group by a ratio of 4.5:1, where bends from 20-35° stop rupture by about 2:1 (sum the respective weights from **Figure 7b**). At this level of simplification, the dip-slip passing ratio is grossly similar to the strike-slip result. A larger sample size would be needed to tell whether this result is real or an accident of the sample.

Other Rupture Complexities.

The collected surface rupture maps of BW16 and W08 provide a basis for evaluating the relative frequency of other types of complexity in surface ruptures. Taking a cue from UCERF3, recent ground motion scenarios have begun considering a wider range of fault-to-fault rupture possibilities, and even topologies such as "Y" shapes that even UCERF3 did not include. We consider below the incidence of overlapping rupture, fault-to-fault ruptures, and non-conventional rupture topologies.

Overlapping lengths in surface rupture are observed in rupture maps (BW16, W08), generally in association with release of fault normal stresses. In reverse and normal mechanism ruptures, overlapping rupture commonly occur as sub-parallel secondary failures of the hanging wall. In strike-slip ruptures overlap is less common, and normally associated with steps or larger scale restraining or releasing fault bend structures. Overlap lengths for the combined rupture set are plotted in **Figures 8a** and **8b** as a function of length and rupture magnitude, respectively. To preserve plotting scale, three overlap estimates greater than 100 km (**Table 1**) are not shown. Long strike-slip ruptures generally have smaller fractional overlap compared to shorter ruptures (**Figure 8c**). The prominent exception, at 245 km length and a fractional overlap of 0.8, is the 1957 Gobi-Altai rupture. This earthquake involved significant fault-normal stresses, as indicated by the 10's of km of reverse rupture that extended southwest from the main trace, and by the exceptional dip of ~45 degrees on the main strike-slip fault surface (Choi et al., 2012). Dip-slip ruptures have fractional overlap somewhat larger on average than that of strike-slip ruptures (**Figure 8d)**.

An innovation of UCERF3 was to allow ruptures in the fault system to jump from one fault to another. The rules allowing such connections in the model are summarized in Field et al. (2014) and described in more detail in Milner et al. (2013). A minimum fault-to-fault rupture would involve at least ~14 km (two subsections) on one fault and ~7 km (one subsection) on another. Examples in nature include the 1992 Landers, California earthquake, which jumped in strike slip across steps or shear zones to connect the Johnson Valley, Homestead Valley, Emerson, and Camp Rock faults, and the 2002 Denali rupture, which included reverse motion on the Susitna Glacier fault, and strike-slip on the Denali and Totschunda faults. We use the combined rupture set to evaluate how frequently fault-to-fault ruptures occur. Instances of fault-to-fault rupture in the combined data are listed in **Table 1** and summarized by mechanism type in **Table 2**. In general instances of fault-to-fault rupture were counted as such if the main rupture left an existing trace to continue on a non-contiguous fault either of the same slip sense, or to change slip sense. The number of fault-to-fault cases in **Table 2** reflects the ~7 km scale used in this research. **Table 1** entries for end angles and end distances give some idea of how the compilation could change if shorter lengths were adopted, but examination of the maps would be required to attempt a quantitative revision. We find that fault-to-fault rupture cases tend not to change mechanism, and that among ruptures that do change type, strike-slip transitioning to reverse (events 37, 49, 55, and 66) are most common. Examination of the rupture maps indicates that for at least events 49, 55, and 66, strike-slip transition to reverse structures had the effect of preserving the slip direction through a change in rake angle onto the reverse fault. Strike-slip to normal transfers do occur, but none quite reached the ~7 km scale of our compilation.

Relative frequency of other types of rupture complexity can be estimated from the combined rupture set. For example, "Y" shaped ruptures over ~7 km or more with significant slip on both arms are present in the data set. Depending on mechanism type, the arms may intersect at up to 90°. In Table 1, events 16, 21, 24, 28, 39, 47, and 49 include at least one Y in the surface rupture. Of these, four involve strike-slip only (events 21, 39, 47, and 49 of 42 total), three (events 16, 24, and 28 of 25 total) are purely dip slip, and one (event 49) involves simultaneous strike-slip and reverse motion. Recognizing that the sample size is small, it appears that fewer than 10% of strike-slip ruptures in our collection have significant "Y" shaped ruptures, while slightly more than 10% of dip-slip ruptures include them. If the criteria for complexity is extended to include extensive fracturing and/or discontinuous rupture of the hanging wall, 6 of 14 normal events (events 5, 14, 16, 41, 53, and 75) and 5 of 11 reverse ruptures (events 4, 28, 40, 55, and 69) would be included. Thus almost half of dip-slip ruptures in our compilation have significant complexity expressed as secondary fault offsets in the hanging wall.

These relative frequencies affect seismic source characterization in PSHA because probabilities must be assigned to various rupture scenarios, including the non-conventional ones. The relative frequency of rupture complexities also affects how much attention to give the scenario in the ground motion characterization phase. Results here are intended to summarize our map interpretations at the project scale length of ~7 km. Projects with interests at other scales are advised to refer to the original map data

Discussion

Empirical measurements from actual surface ruptures provide fundamental data for comparison with numerical simulations and fault theoretical models. Our measurements are an initial first-order synthesis. For almost all of these events, more might be learned from a more in-depth analysis. For example, plotting the rupture on a digital elevation map would show where slip is producing positive or negative topography, and improve interpretation of rupture bends. Nonetheless, this initial examination provides observations and insight that may be useful to those modeling the earthquake source and those using fault data to assess seismic hazard

The largest interior bends passed in rupture (**Figure 2**) provide perhaps the best direct empirical test of allowable fault mis-alignment relative to fault driving stress. Regional geodetic maps typically find that the strain field varies smoothly on the scale of 10's of km. Bends at ~7 km scale thus generally occur in a nearly constant stress orientation. To propagate through both arms of the bend, they must be at least minimally favorable in orientation. Modeling results of Lozos et al. (2011) suggest an upper limit between 32° and 34°. Our empirical data (**Figure 2**) suggest a limit near 28°. Two apparent exceptions are each associated with local transition to reverse faulting structures, and neither case would be well represented by the Lozos et al. (2011) model. Dip slip ruptures less clearly suggest a corresponding nominal limit near 50° perhaps also due to frictional limitations.

The deflection angles at the ends of ruptures also suggest a nominal limit near 50° for both dip-slip and strike-slip mechanisms (**Figure 3**). Since many structures terminating strike slip rupture have or would require normal or reverse slip, a common limit may reasonably be expected.

Net angular deflection in ruptures measure how far in orientation that one end of a rupture can be from the other (**Figure 4**). Like the corresponding maximum interior bends, net angular deflection angles concentrate below ~30° and 50°, for strike slip and dip slip ruptures, respectively. We suggest from this agreement that stress field orientation for most ruptures is grossly constant for ruptures of 10's of km in length as well. For ruptures 100's of km in length, actual rotation of the stress field can occur, in which case the parallel between net angular deflection and maximum interior bends no longer applies. Observed net angular deflection in Figure 4 can be compared to the UCERF3 limit of 60° (Milner et al., 2013). We find that 95% of strike slip ruptures end within 40° of their starting orientation (Figure 4b), suggesting that UCERF could consider a lesser limit. On the other hand, for dip slip a 60° limit would have excluded approximately 15% of actual ruptures.

Total absolute angular deflection can be interpreted as one measure of overall rupture complexity. Each bend alters the energy balance between frictional losses, potential energy, and elastic and inelastic rock mechanical energy. Ruptures with a large TAAD

have overcome more and/or larger bends, and thus more circumstances with the potential to arrest dynamic rupture. We find that TAAD increases in some strike slip ruptures longer than 150 km (**Figure 5a**), but many do not. Thus ruptures can grow in length without overcoming more bends. Biasi and Wesnousky (2016) found a similar relationship of long ruptures to the number of internal steps overcome. Across both rupture mechanisms, only the 1957 Gobi Altai and 2008 Wenchuan ruptures have TAAD values over 250°. UCERF3 allowed TAAD in ruptures up to 560° (Milner et al., 2013). Data in **Figure 5** may be useful for assessing model rupture credibility in future rupture forecasts.

The separation between strike slip and dip slip mechanism ruptures is clearest when plotted in terms of average curvature (Figure 5d). Strike slip ruptures with largest average curvature are shorter than 100 km and occur in extremely complex tectonic environments. Dip slip rupture TAAD curvature exceeds that of strike slip by roughly 3:1. This difference can be qualitatively interpreted in terms of the difference in slip vector direction relative to the bend. For strike slip earthquakes, bends directly impact friction and rupture energy balance, where dip slip on a corrugated fault with high TAAD can be mechanically compatible.

Statistics of bends in fault rupture traces can help set probabilities of future fault rupture extent. **Figure 6** makes clear that bends will have higher predictive power for strike slip ruptures than for dip slip ruptures. Ending angles in **Figure 6a** form a distinct population from interior bends, with larger angles at all cumulative distribution points. Dip slip bends do not separate so clearly. Bends ending rupture are systematically larger than interior bends up to about 20°, but distributions are otherwise fairly similar.

Differences between mechanisms carry forward to estimates of passing ratios as a function of bend angle (Figure 7) that have been developed from the observations summarized in Figure 6. From an approximate relation $PR = Passing\ Ratio = 3.0 - 0.077A$, bends in strike-slip ruptures of $A = 26°$ are equally likely to stop ruptures or to be passed. Lozos et al. (2011) suggest a limit between 18° and 34° below which ruptures are generally successful. The coincidence between observations and the averaged bounds from their study suggests to us that the simplified model of Lozos et al. (2011) is representative of the behavior of real faults. The proposed passing ratio relation is based on the ~7 km scale lengths used in this project, and might need to be adjusted for application to finer or larger scale bend features.

Simple Physical Model

Fault bends affect the energy balance of earthquake ruptures by changing the friction that must be overcome on the fault and by changing the strain energy density in the rock away from the fault. We use a simple ramp model to isolate the friction effects of a bend in a fault trace (Jaeger and Cook, 1979, p.54). **Figure 9** shows friction amplification versus bend angle for coefficients of friction μ=0.3 and 0.6. These values, also used by Lozos et al. (2011), can be considered a representative range between static and dynamic friction.

If we compare friction amplification to the passing fraction in **Figure 7**, some patterns may be observed. For angles up to ~13 degrees, the passing ratio is 2:1. At this angle the frictional amplification is between 27% and 36% compared to a straight fault. Amplification at 26°, where at a passing ratio of 1, amplifications are 62% and 84%, respectively. At 32° ruptures end with a ratio of 2:1. In this range friction is amplified between 85% and 140%. From these observations we can identify a range roughly between 40% and 85% where friction begins to strongly affect rupture propagation. In this we must assume that regional stress orientation effects have in some sense been averaged out in the passing ratio. If the regional stress orientation is known relative to a fault of interest, the angle relations to friction thresholds in **Figure 9** can be adjusted accordingly. Recognizing that other variables also contribute, and that the model we use is very simple, it appears that useful limits on fault friction can be proposed based on our rupture bend tabulation.

Conclusions

Probabilities of propagation through fault bends compliment the recent similar examination of steps as fault geometric factors for improving seismic hazard assessment through improved relative probabilities among candidate rupture hazards. Empirical measurements from bends in historical surface ruptures also show systematic relationships of potential use in seismic hazard analysis. Bend angles at rupture termination are systematically larger for strike-slip earthquakes than interior bends overcome during rupture. The relative frequencies in these populations reveal a systematic relationship between bend angle and the probability that rupture will pass through. A simplified physical model of slip in a fault bend as a ramp suggests that the relationship can be explained by the increase in frictional resistance with increasing bend angle. Dynamic models of rupture lead to similar conclusions. Empirical data provide an observational basis to improve these models.

Dynamic models such as in Lozos et al. (2011) have the advantage of operating under strictly prescribed physical conditions and a precisely known state and orientation of fault driving stress. These circumstances lead to sharply defined boundaries separating bend angles passed or not passed during rupture. On the other hand, the empirical data do not offer such sharp bounds, and passing or not passing a given bend can only be described in probabilistic terms. The difference between these results traces to parameters that are not available in the empirical data. A clear factor is the orientation of rupture driving stress relative to the fault bend. Lozos et al. (2011) show that changes of 10° produce much larger shifts in favorability, and the amount of the shift depends on whether the bend is compressional or dilational. We have not controlled for this distinction, so the consequent variability leads to inconsistent passing and an uncertain function of the bend angle. Other factors also contribute uncertainty, including past rupture history, the location of the hypocenter relative to the bend, fault frictional property variations, three-dimensional geology and interactions with other faults. The passing ratio developed here should be interpreted as an empirical probability relationship that averages through these effects.

Not unexpectedly, properties of bends in dip slip and strike slip ruptures differ significantly. Bends in strike slip ruptures have direct consequences for frictional resistance, while the slip vector orientation in dip-slip ruptures does not necessarily conflict with the bend. Maximum interior bends and net deflection of rupture ends both indicate stiffening mechanical resistance for strike slip bends above 30°, while the corresponding stiffening for dip-slip ruptures is nearer to 50°. By combining passing fractions of bends from 5-20° to those of 20-35°, a passing ratio similar to that for strike slip is suggested. If real, the similarity may reflect similar frictional effects as seen with strike-slip ruptures, but a larger sample size or focused dynamic modeling will be required to say more.

The present survey of surface ruptures poses a challenge to models of rupture as being linear and simply connected. Especially among dip slip ruptures, fault offsets frequently occur in the hanging wall and away from the main rupture trace. Reverse slip events are observed to sometimes include spatially disconnected conjugate ruptures. Y-shaped topologies and rupture splays are noted in a significant though minority of ruptures. Ruptures also commonly include up to 20% of their length in overlapping ruptures. This raises the question, not addressed here, of how important rupture topological complexity is for ground motion estimation. For example, some rupture overlap may be secondary, but the 2011 Fukushima-ken Hamadori earthquake has nearly an overlapping structure, and the overlapping part clearly had ground motion consequences (Anderson et al., 2012).

Our tabulation of incidence of fault-to-fault rupture is closely tied to the single scale length of ~7 km adopted for the measurements. Fault-to-fault instances strongly concentrate in jumps to another fault with the same slip mechanism, as predicted by the effects of stress orientation on rupture favorability. Even in the cases where fault-to-fault jumps change slip mechanism, the jump is not to slip in an entirely a new direction, but often continues slip on a compatible surface in nominally the same direction. These findings may be useful in setting rules for candidate ruptures of a future forecast such as UCERF.

Data and Resources

Surface rupture maps used for measurements of bends, ending complexities, and rupture overlap and associated metadata were from Biasi and Wesnousky (2016) and Wesnousky (2008). Digital format line drawings for angle and overlap measurements are available from the authors.

Acknowledgements

Primary research was funded through USGS National Earthquake Hazard Reduction Program External Grant G14P00068. Additional support through SCEC 2015 Award #15205 is gratefully acknowledged. This is SCEC Contribution #7056.

Bibliography of Publications From This Work

This report is currently in review at the Bulletin of the Seismological Society of America.

References

Anderson, G., B. Aagaard, and K. Hudnut (2003). Fault interactions and large complex earthquakes in the Los Angeles area, *Science*, **302,** 1946–1949.

Anderson, J. G., H. Kawase, G. P. Biasi, J. N. Brune, and S. Aoi (2013). Ground motions in the Fukushima-Hamadori, Japan, normal-faulting earthquake, *Bull. Seism. Soc. Am.,* **103,** 1935-1951.

Ando, R., Shaw, B.E., Scholz, C.H., 2009. Quantifying Natural Fault Geometry: Statistics of Splay Fault Angles. *Bull. Seism. Soc. Am.*, **99,** 389-395.

Aochi, H., R. Madariaga, and E. Fukuyama (2002). Effects of normal stress during rupture propagation along nonplanar faults, J. Geophys. Res. **107,** doi 10.1029/2001JB000500.

Bhat, H.S., Olives, M., Dmowska, R., Rice, J.R., 2007. Role of fault branches in earthquake rupture dynamics. *J. Geophys. Res.,* **112,** B11309, doi:10.1029/2007JB005027.

Biasi, G. P., T. Parsons, R. J. I. Weldon, and T. Dawson (2013). Fault-to-fault rupture probabilities, *U.S.G.S. Open-File Report 2013-1165, Uniform California Earthquake Rupture Forecast Version 3 (UCERF3) , The Time-Independent Model, Appendix J,* 20 pp.

Biasi, G. P., and S. G. Wesnousky (2016). Steps and gaps in ground ruptures: Empirical bounds on rupture propagation, *Bull. Seism. Soc. Am.*, **96**, 1110-1124.

Choi, J-H., K. Jin, D. Enkhbayar, B. Davvasambuu, A. Bayasgalan, and Y.-S. Kim (2012). Rupture propagation inferred from damage patterns, slip distribution, and segmentation of the 1957 M-W 8.1 Gobi-Altay earthquake rupture along the Bogd fault, Mongolia, *J. Geophys. Res.*, **117**, 1-24.

Duan, B., and D. D. Oglesby (2006). Heterogeneous fault stresses from previous earthquakes and the effect on dynamics of parallel strike-slip faults, *J. Geophys. Res.*, **111**, B05309.

Field, E. H., R. J. Arrowsmith, G. P. Biasi, P. Bird, T. E. Dawson, K. R. Felzer, D. D. Jackson, K. M. Johnson, T. H. Jordan, C. Madden, A. J. Michael, K. R. Milner, M. T. Page, T. Parsons, P. M. Powers, B. E. Shaw, W. R. Thatcher, R. J. Weldon, and

Y. Zeng (2014). Uniform California Earthquake Rupture Forecast, Version 3 (UCERF3), "The Time Independent" Model, *Bull. Seism. Soc. Am.*, **104,** 1122-1180.

Fliss, S., Bhat, H.S., Dmowska, R., Rice, J.R., 2005. Fault branching and rupture directivity. *J. Geophys. Res.,* **110,** B06312, doi:10.1029/2004JB003368.

Harris, R. A., R. J. Archuleta, and S. M. Day (1991). Fault steps and the dynamic rupture process: 2-d numerical simulations of a spontaneously propagating shear fracture, *Geophys. Res. Lett.*, **18,** 893–896.

Harris, R. A., and S. M. Day (1993). Dynamics of fault interaction: Parallel strike-slip faults, *J. Geophys. Res.*, **98**, 4461-4472.

Jaeger, J. C., and N. G. W. Cook (1979). Fundamentals of Rock Mechanics, Chapman and Hall, London.

Kase, Y., and S. M. Day (2006). Spontaneous rupture processes on a bending fault, *Geophys. Res. Lett.*, **33** 1-4.

Lettis, W., J. Bachhuber, R. Witter, C. Brankman, C. E. Randolph, A. Barka, W. D. Page, and A. Kaya (2002). Influence of releasing step-overs on surface fault rupture and fault segmentation: Examples from the 17 August 1999 Izmit earthquake on the North Anatolian fault, Turkey, *Bull. Seism. Soc. Am.*, **92**, 19-42.

Lozos, J. C., D. D. Oglesby, J. N., Brune, and K. B. Olsen (2014). Rupture propagation and ground motion of strike-slip stepovers with intermediate fault segments, *Bull. Seism. Soc. Am.*, **104**, 387-399.

Lozos, J. C., D. D. Oglesby, B. Duan, and S. G. Wesnousky (2011). The effects of double fault bends on rupture propagation: A geometrical parameter study, *Bull. Seism. Soc. Am.*, **101,** 385-398.

Milner, K. R., M. T. Page, E. H. Field, T. Parsons, G. P. Biasi, and B. E. Shaw (2013). Defining the inversion rupture set using plausibility filters, *U.S. Geological Survey Open File Report 2013-1165, Appendix T*, 14 pp.

Oglesby, D. D. (2005). The dynamics of strike-slip step-overs with linking dip-slip faults, *Bull. Seism. Soc. Am.*, **95**, 1604-1622.

Oglesby, D. (2008). Rupture termination and jump on parallel offset faults, *Bull. Seism. Soc. Am.*, **98**, 440-447.

Saucier, F., E. D. Humphreys, and R. J. I. Weldon (1992). Stress near geometrically complex strike-slip faults: Application to the San Andreas Fault at Cajon Pass, southern California, *J. Geophys. Res.*, **97** 5081-5094.

Scholz, C. H. (2002). The Mechanics of Earthquakes and Faulting, Second Edition, Cambridge University Press, Cambridge, 471 pp.

Scholz, C.H., Ando, R., Shaw, B.E., 2010. The mechanics of first order splay faulting: The strike-slip case. *J. Struct. Geol.*, **32**, 118-126

Wesnousky, S. G. (2008). Displacement and geometrical characteristics of earthquake surface ruptures: Issues and implications for seismic-hazard analysis and the process of earthquake rupture, *Bull. Seism. Soc. Am.*, **98** 1609-1632.

Wesnousky, S.G., 2006, Predicting the endpoints of earthquake ruptures: *Nature*, **444**, 358-360.

Zhou, R. Q., W.-X. Yu, Y.-S. Gu and X. Z. Yao (1990). A study of the rupture zone of the 1988 Gengma earthquake with magnitude 7.2 in Yunnan Province, *Seismology and Geology*, **12**, 291-302 (in Chinese).

Table 1. Bend Angles and Complexities

Enum	Events from Wesnousky (2008)	Mech-anism	Surface Rupture Length	Magnitude	end1 angle	end1 dist	end2 angle	end2 dist	fault to fault	over-laps	squirrel	net deflection	Internal bend		Complexities and Notes
1	09 Jan 1857 Ft Tejon, California	S	339	7.9	0		0		no	0	108	18	17	4, 8, 7, 14, 14, 10, 17, 17, 4, 3, 3, 7	-
2	03 May 1887 Sonora (Pitacayachi), Mexico	N	102	7.5	-1		-1		N-N	0	207	23	45	43, 25, 43, 22, 45, 12, 17	5 km step, 7 km gap to Otates fault
3	28 Oct 1891 Neo-Dani, Japan	S	80	7.3	-2		16	0	SS-SS	0	109	31	28	16, 28, 6, 25, 23, 11	Neodani on strike with Umehara fault; not included as fault-to-fault
4	31 Aug 1896 Rikuu, Japan	R	37	7.2	35	5	-1		R-R	0	65	7	36	29, 36	R-R across 12 km step to opposite vergence rupture; R-R across 8 km step
5	02 Oct 1915 Pleasant Valley, Nevada	N	61	7.3	-1		20	5	N-N, N-N	4	46	23	20	14, 12, 20	4, 7 km steps; fractured hanging wall
6	02 Nov 1930 Kita-Izu, japan	S	35	6.7	34	4	82	5	no	8	28	28	28	28	terminal rupture occurs on conjugate SS fault
7	26 Dec 1939 Erzincan, Turkey	S	300	7.7	-1		-1		no	20	69	25	16	16, 8, 8, 2, 12, 23	-
8	19 May 1940 Imperial, California	S	60	6.9	25	3	0		no	0	29	1	15	7, 15, 7	-
9	20 Dec 1942 Erbaa-Niksar, Turkey	S	28	6.8	18	3	0		no	0	37	7	22	15, 22	-
10	26 Nov 1943 Tosya, Turkey	S	275	7.6	34	2	19	0	no	0	41	41	16	2, 16, 9, 8, 6	-
12	01 Feb 1944 Gerede-Bolu, Turkey	S	155	7.4	13	8	0		no	4	34	4	19	15, 19	-
14	16 Dec 1954 Dixie Valley, Nevada	N	47	6.8	0		38	0	no	15	196	30	96	17, 35, 96, 48	shattered hanging wall piedmont
15	16 Dec 1954 Fairview Peak, Nevada	N	62	7.0	21	3	27	4	no	3	8	8	8	8	total deflection much larger at smaller length scale; SS slip comparable to N
16	18 Aug 1959 Hegben Lake, Montana	N	25	7.0	24	2	30	0	N-N	8	124	4	64	60, 64	5 km step, Y topology
17	22 Jul 1967 Mudurnu Valley, Turkey	S	60	6.7	-2		0		no	0	28	28	15	15, 13	-
18	09 Apr 1968 Borrego Mountain, California	S	31	6.1	-2		12	0	no	0	48	12	21	9, 18, 21	-
19	01 Feb 1971 San Fernando, California	R	15	6.7	-1		27	2	no	0	28	28	28	28	-
21	15 Oct 1979 Imperial Valley, California	S	36	6.3	43	2	0		no	0	7	7	7	7	Y topology on 12 km splay on NW end at 36 degrees
22	10 Oct 1980 El Asnam, Algeria	R	27.3	6.7	31	1	31	4	no	0	13	13	13	13	-
23	29 Jul 1981 Sirch, Iran	S	64	6.4	43	7	6	3	no	37	38	16	27	11, 27	Extensive parallel ruptures off main trace
24	28 Oct 1983 Borah Peak. Idaho	N	34	6.9	14	1	28	2	no	13	82	62	48	48, 10, 24	Y topology, 2 arms 13 km; overlap is 1 arm of Y
25	03 Mar 1986 Marryat, Australia	R	13	5.9	-1		-1		no	0	103	103	103	103	conjugate SS ruptures
26	02 Mar 1987 Edgecumbe, New Zealand	N	15.5	6.3	50	2	-1		N-N, N-N	6	ND	ND	ND		N-N across 8 km and 3 km; hanging wall widely fractured; retained as 15 km rupture with main phase stopping at a bend.
27	23 Nov 1987 Superstition Hills, California	S	25	6.2	15	3	16	2	no	4	21	21	13	13, 8	-
28	22 Jan 1988 Tennant Creek, Australia	R	30	6.6	-1		-1		R-R	0	42	42	42	42	Y topology; 6 km step, vergence reversal
29	16 Jul 1990 Luzon, Philippines	S	112	7.6	25	3	22	4	no	0	91	11	26	26, 18, 11, 22, 14	-
30	28 Jun 1992 Landers, California	S	63.2	7.2	20	2	0		SS-SS, SS-SS,	25	103	47	28	18, 28, 21, 15, 21	3 SS-SS jumps; extensive shear overlap.
31	14 Mar 1998 Fandoqa, Iran	S	25	6.6	14	2	6	0	no	6	0	0	0	0	-
32	21 Sep 1999 Chi-Chi, Taiwan	R	72	7.4	41	2	0		no	12	242	34	46	43, 30, 46, 46, 19, 19, 39	-
33	12 Nov 1999 Duzce, Turkey	S	40	7.0	17	4	28	3	no	0	23	23	12	12, 11	-
34	17 Aug 1999 Izmit, Turkey	S	107	7.1	6	0	17	0	no	15	31	15	23	8, 23	-
35	16 Oct 1999 Hector Mine, California	S	44	6.9	-2		23		no	22	75	21	27	22, 27, 26	parallel secondary zones on SE end of rupture
36	14 Nov 2001 Kunlun, China	S	421	7.8	0		-1		SS-SS	60	75	11	12	12, 11, 9, 6, 8, 5, 6, 9, 9	TAAD is minimum because of map scale
37	03 Nov 2002 Denali, Alaska	S	341	7.9	7	0	-1		SS-R, SS-SS	10	142	40	40	27, 40, 17, 8, 9, 26, 9, 6	SS-R at Susitna Glacier-Denali fault intersection; SS-SS at Denali-Totschunda fault
	Events from Biasi and Wesnousky (2016)														
38	02 Feb 1892 Laguna-Salada, Baja, CA	S	42	7.2	75	5	-1		no	0	19	11	15	15, 4	3 km prominent normal fault terminal ending
39	23 Jul 1905 Bulnay, Mongolia	S	375	8.4	18	7	-1		SS-SS, SS-SS	102	50	5	15	15, 11, 4, 7, 4, 4, 5	Y topology to SS for 82 km, SS-SS conjugate for 20 km; SS-SS in Y's is not in squirrel or IB
40	03 Jan 1911 Chon-Kemin (Kebin), Kyrgyzstan	R	177	7.7	-1		-1		R-R	25	73	44	31	31, 13, 16, 13	10 km step; extensive overlaps
41	13 Jan 1915 Avezzano, Italy	N	40	7.0	20	4	-1		N-N, N-N	9	15	15	15	15	4, 7 km steps; hanging wall fractured
42	16 Dec 1920 Haiyuan, China	S	237	8.3	-1		-1		no	15	128	22	28	25, 21, 20, 28, 13, 21	TAAD is minimum

43	7 Mar 1927	Tango, Japan	S	35	7.0	88	0	-1	no	1	10	10	10	10	4 km gap; 8.5 km at right angles separated from main rupture
44	06 Jan 1928	Laikipia - Subukia Kenya	N	40	6.9	71	3	-1	no	3	39	39	39	39	-
45	10 Aug 1931	Fuyun, China	S	160	7.9	16	5	-1	no	32	146	4	24	12, 12, 12, 17, 8, 12, 16, 24, 18, 15	-
46	25 Dec 1932	Changma, China	S	149	7.6	44	11	40	10 no	28	31	5	18	18, 13	oblique normal and reverse terminations at high angles; very complex surface rupture
47	18 Mar 1953	Yenice-Gonen, Turkey	S	60	7.2	34	0	48	5 no	9	53	3	25	15, 13, 25	Y structure at east end, arms 6 and 7 km.
48	09 Feb 1956	San Miguel, Mexico	S	20	6.7	37	1	-1	no	0	11	11	11	11	-
49	04 Dec 1957	Gobi-Altai, Mongolia	S	245	8.0	39	10	67	5 SS-R, SS-SS	196	257	15	55	11, 23, 19, 15, 38, 55, 24, 19, 36, 10, 7	163 km+ in Gurvan Bulag Thrust, Y-topo (2x), 20 km on conjugate SS fault
50	01 Sep 1962	Buyin Zara (Ipak fault), Iran	S	103	7.2	56	8	23	2 no	2	47	3	25	25, 22	steps, reverse and normal structures at <5 km scale
51	05 Jan 1967	Mogod, Mongolia	S	48.5	7.1	11	1	50	8 no	0	37	17	27	27, 10	southern end reverse structure interpreted as ending rupture.
52	31 Aug 1968	Dasht-e-bayaz, Iran	S	74	7.1	98	9	-2	no	20	29	5	17	12, 17	east end: conjugate slip on syncline
53	28 Mar 1970	Gediz, Turkey	N	40	7.2	-1		51	1 N-N	15	120	68	57	37, 57, 26	15 km of hanging wall offsets and overlapping rupture
54	19 Dec 1977	Bob-Tangol, Iran	S	20	5.9	-1		-2	no	0	4	4	4	4	-
55	16 Sep 1978	Tabas, Iran	R	95	7.3	58	0	-1	R-SS	75	114	16	44	21, 22, 6, 44, 21	2 gaps, 6, 7 km; S end hanging wall broken in 4 reverse tiers; transition to SS on north end
56	27 Nov 1979	Khuli-Buniabad, Iran	S	55	7.0	75	4	-1	no	0	25	1	13	13, 12	-
57	23 Nov 1980	Irpinia, Italy	N	40	6.9	28	5	20	3 no	0	12	12	12	12	6, 4 km gaps, SE end deflection same if measured from the San Gregorio section
58	24-25 Feb 19	Gulf of Corinth, Greece	N	14	6.6	48	3	30	2 no	5	0	0	0	0	-
59	04 Mar 1981	Gulf of Corinth, Greece	N	13	6.4	39	1	-1	no	0	72	12	42	42, 30	rupture short; retained because rupture well described by bends
62	06 Nov 1988	Gengma, Yunnan, China	S	24	6.9	8	2	-1	no	2	21	21	21	21	Interpreted from more detailed map of Zhou et al, 1990
63	07 Dec 1988	Spitak, Armenia	R	20	6.7	-1		-1	no	2	60	4	32	28, 32	-
64	20 Jun 1990	Rudbar, Iran	S	80	7.4	11	0	-1	no	7	32	6	11	7, 6, 11, 8	-
65	27 May 1995	Neftegorsk (Sakhalin), Russia	S	36	7.0	33	0	30	0 no	0	18	18	18	18	-
66	10 May 1997	Zirkuh, Iran	S	125	7.2	42	11	-2	SS-R	21	106	21	27	27, 23, 24, 17, 15	11 km of paired reverse structures
68	08 Oct 2005	Kashmir, Pakistan	R	75	7.6	-1		-1	no	0	67	7	37	37, 14, 16	-
69	12 May 2008	Wenchuan, China	R	240	8.0	-1		-1	R-R	115	273	1	43	8, 21, 8, 43, 41, 19, 40, 35, 34, 14, 10	85 km overlap on Pengguan fault
71	04 Apr 2010	Sierra Mayor - Cucapah, Mexico	S	108	7.2	35	4	-1	SS-SS	12	51	5	14	14, 14, 10, 13	NE dip transitions to SW dip; 8-10 km internal gap/wrench structure
72	14 Apr 2010	Yushu, China-1	S	32	6.8	-2		27	2 no	2	43	21	32	11, 32	-
74	04 Sep 2010	Darfield, New Zealand	S	29.5	7.0	33	4	-1	no	2	8	8	8	8	-
75	11 Apr 2011	Iwaki, (Fukushima-ken Hamadori), .	N	29	6.7	0		8	3 N-N	0	153	147	141	6, 141, 6	Outer angle between faults chosen to follow line of rupture north on Itozawa then south on Yunodake

Note: 0 on end means rupture ends in straight fault section
end angle=0 means flt continues
end angle = -1 means no data/can't tell
end angle -2 means end of fault
ND: No data

Table 2. Fault-to-fault rupture cases

Mechanism	SS	Reverse	Normal	Any
SS	10	4	0	14
Reverse	4	5	0	9
Normal	0	0	10	10

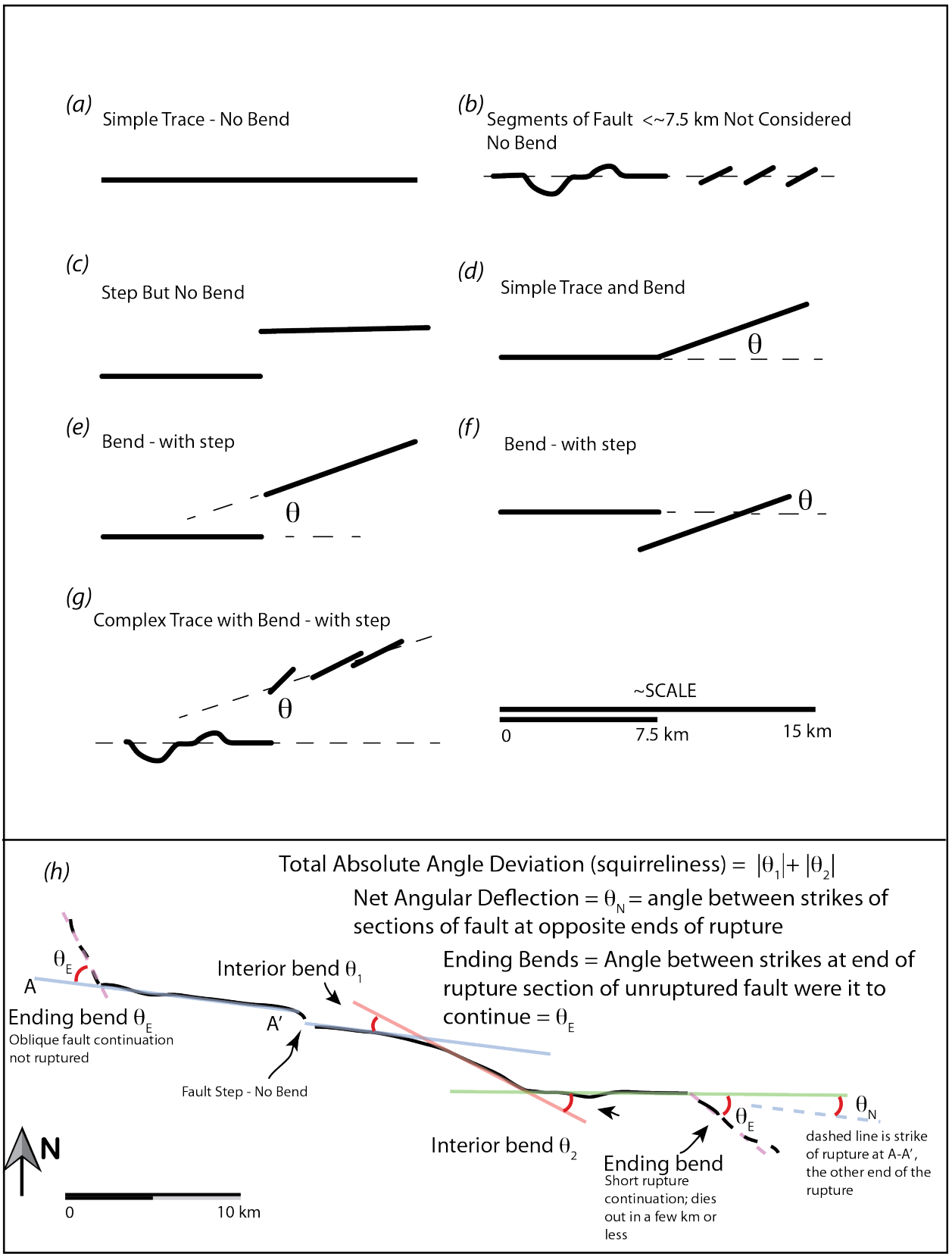
(a)
Simple Trace - No Bend
(b)
Segments of Fault <~7.5 km Not Considered
No Bend
(c)
Step But No Bend
(d)
Simple Trace and Bend
θ
(e)
Bend - with step
θ
(f)
Bend - with step
θ
(g)
Complex Trace with Bend - with step
θ
~SCALE
0
7.5 km
15 km
(h)
Total Absolute Angle Deviation (squirreliness) = |θ1|+ |θ2|
Net Angular Deflection = θN = angle between strikes of sections of fault at opposite ends of rupture
Ending Bends = Angle between strikes at end of rupture section of unruptured fault were it to continue = θE
θE
A
Ending bend θE
Oblique fault continuation not ruptured
Interior bend θ1
A'
Fault Step - No Bend
Interior bend θ2
Ending bend
Short rupture continuation; dies out in a few km or less
θE
θN
dashed line is strike of rupture at A-A', the other end of the rupture
N
0
10 km

Figure 1. Measuring bends and deflections. Upper panel isolates example rupture bend and discontinuity cases. Bends occur at all scales, but measurements for this project are generally relative to a ~7 km scale length. (a) undeflected rupture trace; (b) bends in continuous trace and short misaligned sections; (c) Rupture continues parallel or nearly so across a step. No bend is indicated. (d) simple bend; (e, f) Bends where rupture continues on a different trend across a step; (g) Bend across a step with other smaller misaligned features. (h) Geometry for ending and summary bend measures. Ending bends may or may not have short continuations of rupture at a new angle; structurally the bend is interpreted as a terminal structure relative to the main rupture. Net deflection is the orientation difference between ending main trace elements not counting ending bends. Total absolute angle deviation is the sum of absolute values of deflections – i.e., the total of changes in rupture direction.

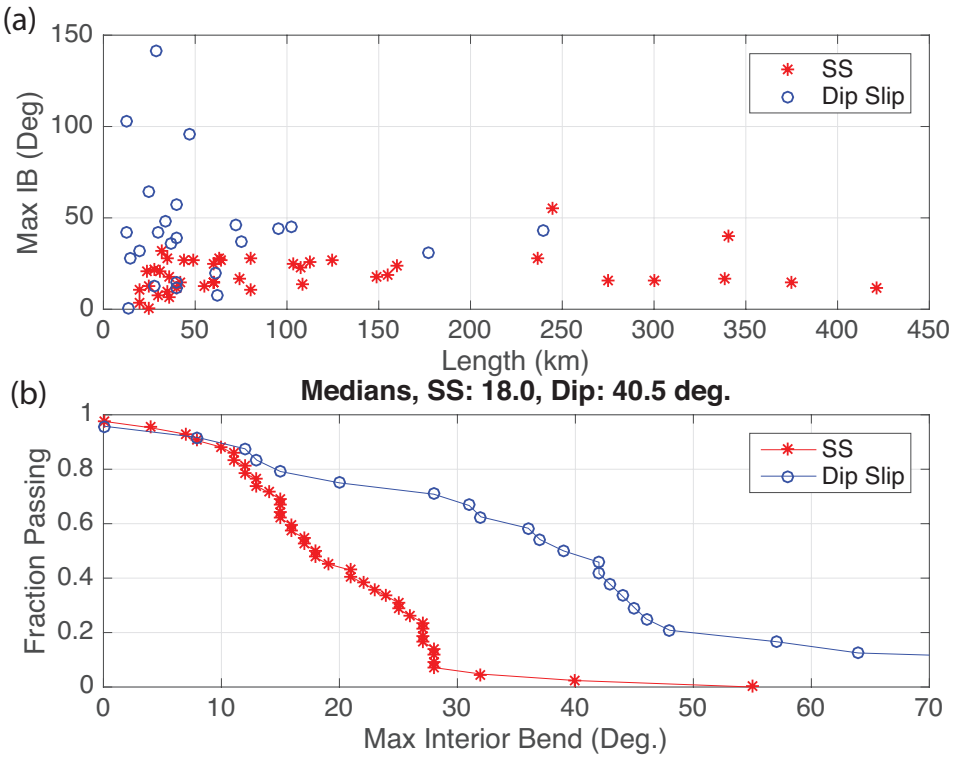

Figure 2. (a) Largest interior bends (Max IB) overcome in strike slip (SS) and dip slip ruptures as a function of rupture length. If rupture dynamic or momentum terms increase with magnitude, larger interior bends might be found in longer ruptures. No strong trend of maximum bends with magnitude is indicated. Strike-slip ruptures rarely pass bends >28 deg. (b) Maximum interior bends for strike slip and dip slip are sorted by size and plotted as fractions greater than the horizontal axis bend angle. To preserve plot scale, the three largest dip-slip points from (a) are not repeated in (b).

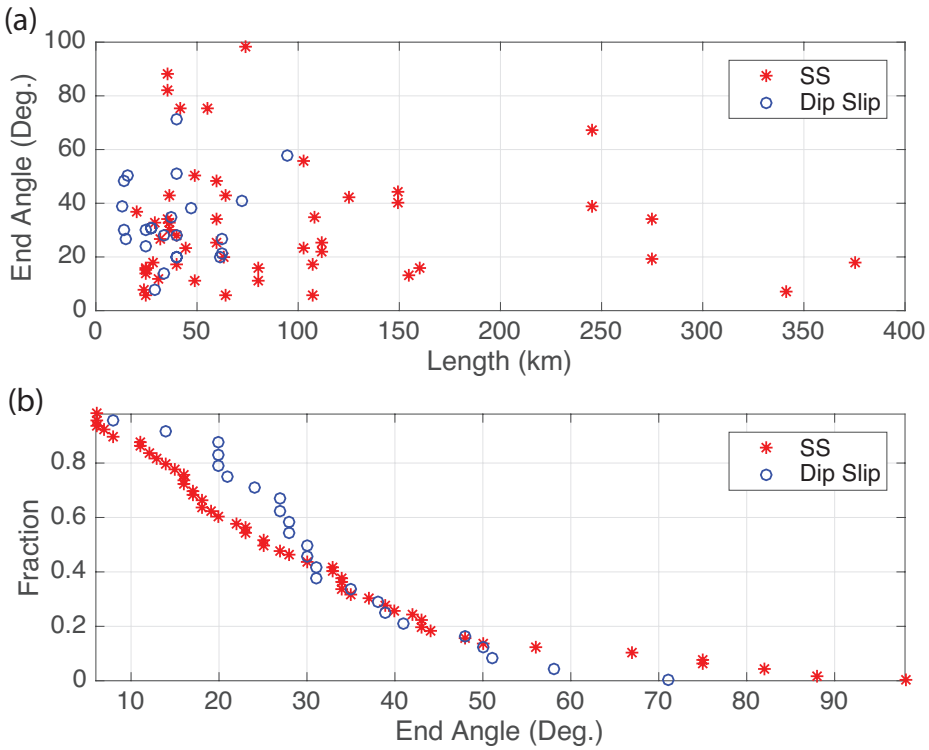

Figure 3. (a) Deflection angles at rupture ends. No clear trend is observed relative to rupture length. (b) Rupture ending angles are sorted and shown as the fraction greater than the horizontal angle axis.

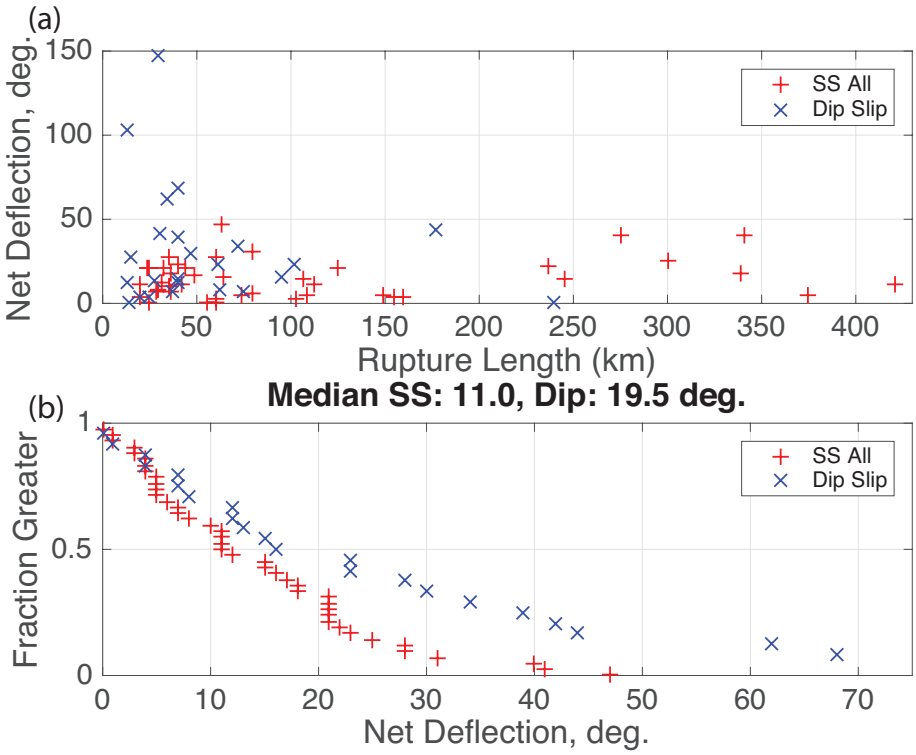

Figure 4. Net deflection angle is the absolute difference in map orientation between ends of ruptures. In (a), net deflection is plotted versus rupture length, with symbols distinguishing dip slip and strike slip ruptures. (b) Complimentary cumulative distribution of net deflection angles. To preserve plot scale, two dip slip points in (a) are not repeated in (b). Median net deflections are 11° and 19.5° for strike slip and dip slip cases, respectively. Only one simple strike-slip rupture exceeds 31° net deflection.

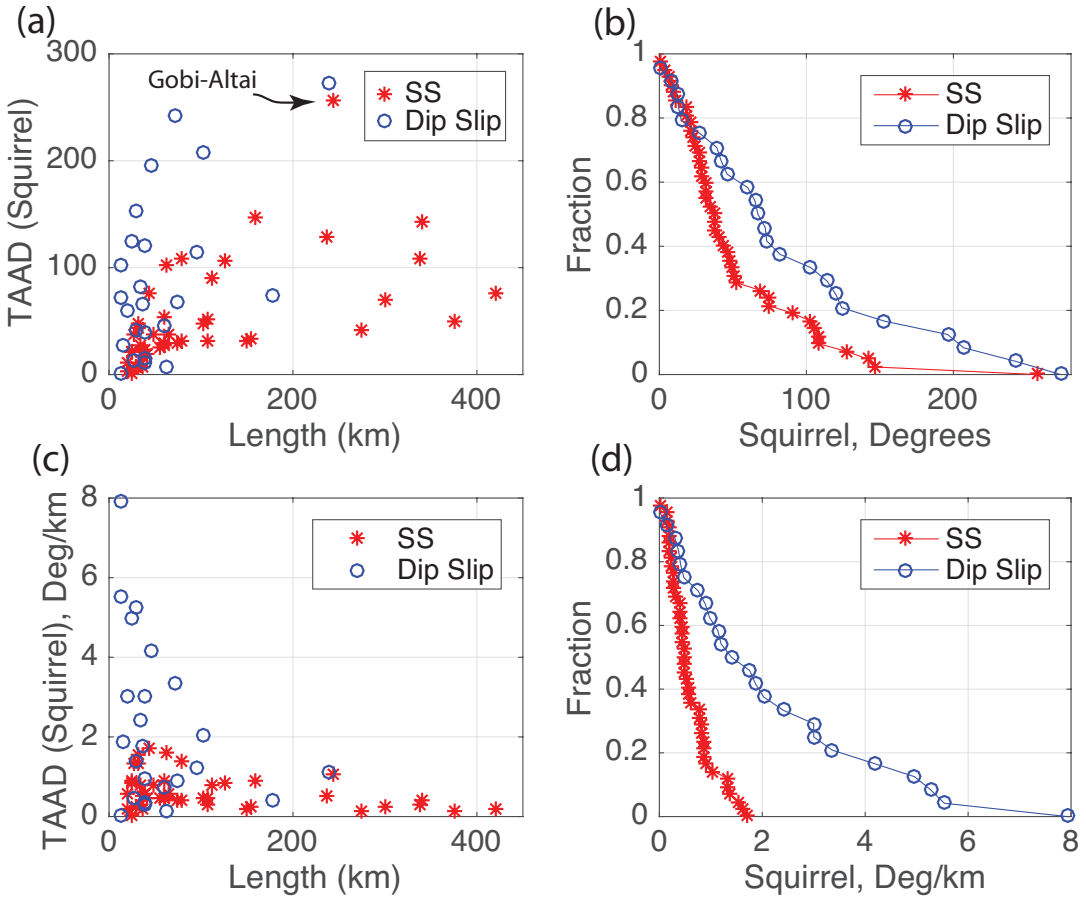

Figure 5. Total absolute angular deflection (TAAD), or "squirreliness", as (a) a function of length; (b) complimentary cumulative distribution showing data fractions greater than a given TAAD; (c) TAAD interpreted as average curvature in units of degrees/km of length; and (d) complimentary cumulative distribution of curvature, in degrees/km. Dip-slip ruptures change direction more by a factor of 3 than strike-slip ruptures.

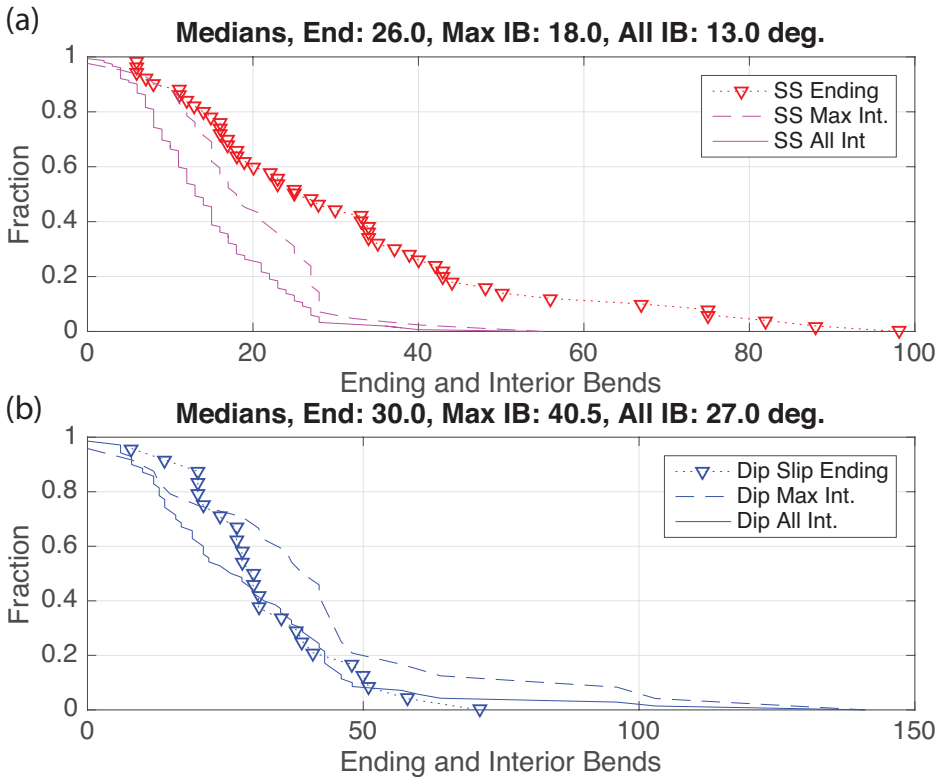

Figure 6. Interior and rupture ending deflection angles for (a) strike slip and (b) dip slip ruptures. Ending measures are shown with symbols; lines only are shown for maximum interior and all interior sets. Fractions refer to the portion of data with a bend larger than the angle on the abscissa.

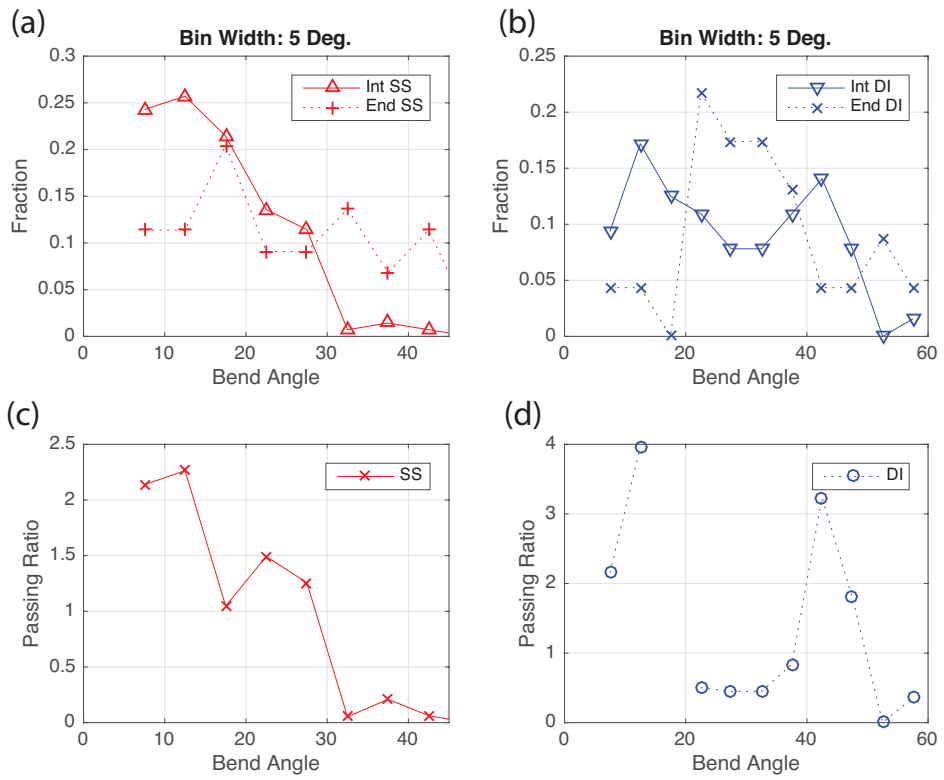

Figure 7. Comparison of data fractions of interior and ending bends for dip-slip and strike-slip bend measurements. (a) Strike-slip bend data, gathered in 5 degree bins. The number of measurements in each bin is divided by the total to get the plotted bin fractions. Bends passed inside ruptures are concentrated below ~20°, while bends ending ruptures are more evenly distributed. One interior bend and many ending bends larger than 45° are not shown (see ***Figure 6****). (b) Dip-slip binned data. (c) Ratio of passed to ending bin fractions for strike-slip. The ratio shows how frequently, as a fraction of its respective type, a bend of a given size is passed. Bends <15° are passed over twice as often as they stop rupture. Bends >30° are twice as likely to stop rupture as to be passed. (d) Dip slip passing ratios are more variable because of small sample size. See text for further discussion..*

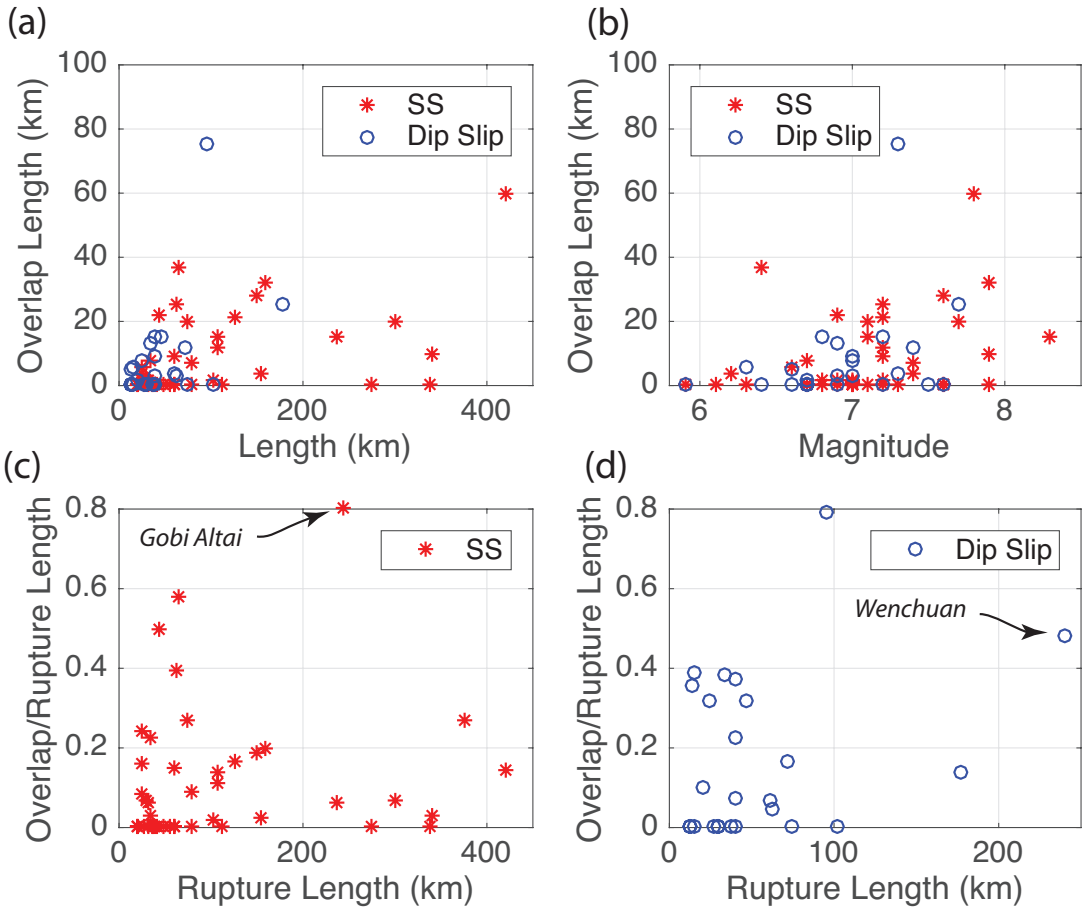

Figure 8. Overlapping rupture length (a) as a function of rupture length; (b) Overlap length as a function of magnitude; (c) fraction of overlap to total length, strike-slip ruptures; and (d) overlap in dip-slip ruptures as a fraction of total length. Three overlap totals longer than 100 km from ***Table 1*** *are not shown in (a) and (b) to preserve plot scale for the majority of the data.*

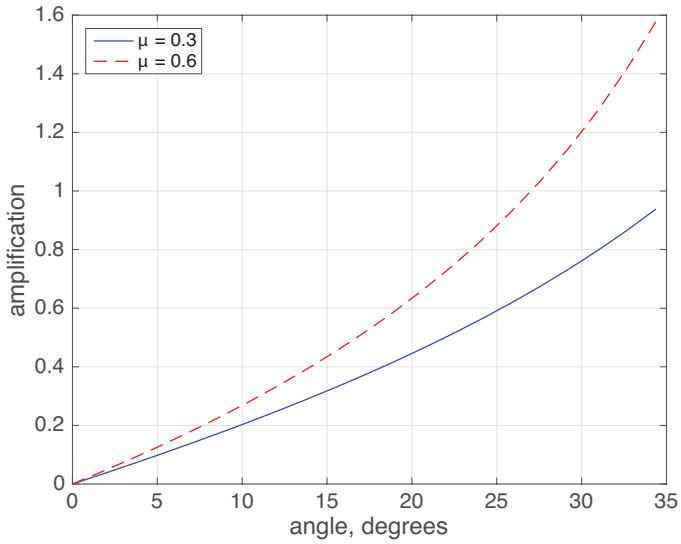

Figure 9. Simplified model of relative increase in frictional resistance on a fault bend for two coefficients of friction μ as a function of bend angle.